

Modeling 2D Arrangements of Graphene Nanoribbons

Talia Tene ¹, Marco Guevara ², Nataly Bonilla García ³, Myrian Borja ³ and Cristian Vacacela Gomez ^{4,*}¹ Department of Chemistry, Universidad Técnica Particular de Loja, Loja 110160, Ecuador² Faculty of Mechanical Engineering, Escuela Superior Politécnica de Chimborazo (ESPOCH), Riobamba 060155, Ecuador³ Escuela Superior Politécnica de Chimborazo (ESPOCH), Riobamba 060155, Ecuador⁴ INFN-Laboratori Nazionali di Frascati, Via E. Fermi 54, I-00044 Frascati, Italy

* Correspondence: cristianisaac.vacacelagomez@fis.unical.it

Abstract: In the last two decades, interest in graphene has grown extensively due to its extraordinary properties and potential for various applications such as sensing and communication. However, graphene is intrinsically a semimetal with a zero bandgap, which considerably delays its use where a suitable bandgap is required. In this context, quasi-one-dimensional counterparts known as graphene nanoribbons (GNRs) have demonstrated sizeable bandgaps and versatile electronic properties, which make them promising candidates for photonic and plasmonic applications. While progress has recently been made toward the synthesis of GNRs, theoretical models to envisage their electronic and optical properties have been restricted to ab initio approaches, which are not feasible for wide systems because of the large number of atoms tangled. Here, we use a semi-analytical model based on Dirac cone approximation to show the adjustable electronic and plasmonic characteristics of wide and experimental GNRs, both freestanding and non-freestanding. This approach utilizes the group velocity of graphene, which is calculated using density functional computations ($v_F = 0.829 \times 10^6 \text{ m s}^{-1}$), as the primary input. Importantly, our research reveals that at the terahertz level, the plasmon-momentum dispersion is highly responsive to changes by varying the ribbon width or charge carrier concentrations, the other involved parameters can be manipulated by setting values from experiments or more sophisticated predictions. In particular, this model can replicate the electronic properties of GNRs on Ge(001) and GNRs on Au(111). From the plasmonic side, the plasmon spectrum of graphene microribbon arrays of $4 \mu\text{m}$ wide on Si/SiO₂ and GNR arrays on Si are found in good agreement with experiments. The potential use of GNRs in sensing molecules such as chlorpyrifos-methyl is also discussed. Chlorpyrifos-methyl is chosen as the test molecule because it is a commonly used insecticide in agriculture, but its high toxicity to organisms and humans makes it a concern. It has been established that the plasmon resonances of all the studied GNRs occur at the same frequency as chlorpyrifos-methyl, which is 0.95 THz. Our findings can serve as a useful guide for future experiments.

Keywords: graphene nanoribbons; DFT; semi-analytical framework; THz

Citation: Tene, T.; Guevara, M.; Bonilla García, N.; Borja, M.; Vacacela Gomez, C. Modeling 2D Arrangements of Graphene Nanoribbons. *Crystals* **2023**, *13*, 311. <https://doi.org/10.3390/cryst13020311>

Academic Editors: Grazia Giuseppina Politano, John Parthenios, Rajratan Basu and Igor Neri

Received: 23 December 2022

Revised: 3 February 2023

Accepted: 10 February 2023

Published: 14 February 2023



Copyright: © 2023 by the authors. Licensee MDPI, Basel, Switzerland. This article is an open access article distributed under the terms and conditions of the Creative Commons Attribution (CC BY) license (<https://creativecommons.org/licenses/by/4.0/>).

1. Introduction

Graphene is a planar sheet of sp²-bonded carbon atoms tightly packed into a honeycomb-like lattice [1,2]. The carbon atoms form a two-dimensional (2D) hybridized network with three nearest neighbors, each at a distance of about 1.420 Å, leaving one unhybridized half-filled p-orbital [3], perpendicular to the graphene plane for every carbon atom. Since 2004 [4], graphene has been the subject of significant research and development, due to its extraordinary electronic, mechanical, thermal, and optical properties [5]. Indeed, graphene has shown a lot of promise for the replacement of silicon-based electronic devices [6]. However, as-found graphene is gapless and cannot be used immediately in up-to-date semiconductor technology because this carbon nanomaterial needs current on/off ratios. Consequently, a great deal of

effort is the opening of a bandgap in graphene without significantly affecting its exceptional properties, particularly, its high electron mobility.

Within this frame of reference, several chemical methods have been proposed, for instance, the oxidation-reduction of graphite to produce graphene derivatives that show optical bandgaps larger than 2 eV [7] or graphenes from microwave-derived carbon precursors for energy savings of up to 60% [8]. These graphene derivatives have the potential for environmental applications [9], advanced composite, and smart (multifunctional) eco-composites [10–12] with applicability in future nanodevices [13,14]. Alternatively, a sizable bandgap can be opened up through the quantum confinement effect by patterning graphene in the form of graphene nanoribbons (GNRs) [15,16]. GNRs are thin and elongated strips with straight edges. As the ribbon width decreases, GNRs can gradually transform from semimetals to semiconductors [17]. As an example, a bandgap of about 100 meV is expected for a ribbon of 10 nm, whereas a ribbon of width ~ 2 nm would have a bandgap of about 1 eV. From a piece of important evidence, Fei Z et al., [18] have reported the successful preparation of GNR samples with widths of $w = 155, 270, 380,$ and 480 nm. Most importantly, based on nano-infrared images, the authors showed the existence of two plasmon modes in experimental GNRs organized as 2D periodic arrays: the conventional surface plasmon and a novel confined (edge) plasmon. Both plasmon modes have been theoretically confirmed in ultra-narrow GNR systems working in the reciprocal space by an ab initio method [19–21].

Plasmons are oscillations of valence electrons on the surface of various materials such as metals, semiconductors, and topological insulators that occur collectively [22]. These collective oscillations can be utilized to control and focus optical energy on a nanometer scale. This is due to the strong interaction between these oscillations and light [23]. In particular, plasmons in graphene reveal high confinement, electrostatic tunability, and long lifetimes [24]. These plasmon features are promising for photonic applications from the terahertz- to the infrared regime. Additional control over surface plasmons has been observed in graphene nanoribbons (GNRs) because of (i) the change in dimensionality from 2D graphene to 1D graphene ribbons and (ii) the confinement of charge carriers [20]. This extra control is expected to be more significant than that of edge plasmons, which is dependent on the bandgap of the GNR [19]. These unique plasmonic properties of GNRs could be utilized to enhance current biosensors that utilize surface plasmon resonance and graphene [25–30].

Previous studies [31,32] have mainly used Time-Dependent Density Functional Theory (TDDFT) within the Random Phase Approximation (RPA) to investigate the plasmonic properties of ultra-narrow GNR arrays (< 2 nm). However, this atomistic approach is not suitable for GNRs of the widths reported in Ref. [18]. In this work, we use an alternative method to examine the electronic and plasmonic properties of experimental GNRs. The proposed semi-analytical model [33] is based on the group velocity of graphene, which is calculated using density functional theory (DFT), as the main input. Both freestanding and non-freestanding systems are considered. We show that the plasmon frequency in wide GNRs is highly sensitive. Additionally, we explore the possibility of using it for sensing chlorpyrifos-methyl. The reason it was picked as the test molecule is that it is widely used in crops as an insecticide, but its harmful effects on living beings and humans raise concerns. Our results can guide the design of future nanodevices based on graphene.

2. Theoretical Framework

It is worth emphasizing that the current modeling approach focuses on the electronic and plasmonic properties of GNRs with widths that have been experimentally observed ($w = 155, 270, 380,$ and 480 nm) [34,35]. The semi-analytical model is composed of two steps:

- (i) Numerical computations using DFT to obtain an accurate group velocity of graphene.
- (ii) Analytical expressions derived mainly from the Dirac cone approximation [33] to investigate the related electronic and plasmonic features.

2.1. DFT Computations

The ground-state properties of graphene were determined by plane-wave DFT computations within the Kohn–Sham formalism implemented in the Abinit software [36]. Electronic structure calculations were performed at the level of local density approximation (LDA) [37] using norm-conserving pseudopotentials to eliminate the core electrons [38]. The plane-wave basis is represented by the space functions:

$$PW_{\mathbf{k}+\mathbf{G}}(\mathbf{r}) = \Omega_0^{-1/2} e^{i(\mathbf{k}+\mathbf{G})\cdot\mathbf{r}} \quad (1)$$

where \mathbf{k} is the wave vector in the first Brillouin zone (Γ KM path) (Figure S1a), \mathbf{G} is the reciprocal-lattice vector, and Ω_0 is the unit-cell volume.

The number of plane waves was limited by the energy-cutoff $|\mathbf{k} + \mathbf{G}|/2 \leq 25$ hartrees (~ 680 eV). The three-dimensional periodicity required by plane-wave DFT was created by repeating the graphene sheets with a distance of 15 Å. Structural optimization was not taken into account in this case as the lattice constant was fixed at 2.460 Å (the case of ideal graphene). The ground-state calculations were carried out using a Γ -centered and unshifted Monkhorst–Pack grid [39] of $90 \times 90 \times 1$ to obtain the complete band structure and density of states (DOS) of graphene (Figure S1b,c), including up to 20 bands. Additionally, a high-resolution Monkhorst–Pack grid of $720 \times 720 \times 1$ was used to obtain the linear band structure of graphene around the K point (Figure S2a), including up to eight bands.

A close picture of the band structure (Figure S1b) shows that graphene exhibits the well-known Dirac cone structure at the K point within ± 0.8 eV around the Fermi energy (E_F) (see Figure S2a). In a simple visual perspective of the density of states (DOS) (Figure S1c) as a function of the energy, one can notice that the two peaks closest to E_F correspond to the π and π^* flat band dispersion at the M point. The other intense peaks are not relevant to the present study since our work is restricted to the Dirac cone. Accordingly, the Monkhorst–Pack grid of $720 \times 720 \times 1$ allows for estimating the limits of Dirac cone approximation and the average charge carrier velocity (v_F , group velocity) of graphene. The latter is the key input parameter of the semi-analytical modeling approach.

By using the high-resolution Monkhorst–Pack grid, the group velocity of graphene was found to be $v_F = 0.829 \times 10^6$ m s⁻¹, which is the average value obtained by linear fitting of the highest valence band ($v_{F-\pi} = 0.827 \times 10^6$ m s⁻¹) and the lowest conduction band ($v_{F-\pi^*} = 0.832 \times 10^6$ m s⁻¹) concerning the magnitude of the wave vector around the K point (Figure S2a). Figure S2b confirms the (quasi) linear variation of the group velocity of graphene for selected values of energy band dispersion. It should be noted that for large values of the wave vector, the band dispersions are anisotropic as a result of the flat band dispersion of the π and π^* bands (± 2 eV).

Even though, if the value of the wave vector gets closer to the dispersion at the K point, the energy band dispersion of the π band (Figure S2c) and π^* band (Figure S2d) deviates slightly from a linear behavior of charge carrier velocity (dashed rectangular regions). This significant finding displays the limit of applicability of the present modeling approach to study, i.e., the semi-analytical model works in an energy range of ± 0.2 eV or about 50 THz.

2.2. Semi-Analytical Model: Estimating the Electronic Properties

As proposed by Popov et al. [33], the linear band dispersion of charge carriers in graphene (near the Fermi energy and around the K point) is the foundation of the semi-analytical model. The group velocities of the π electrons and π^* holes can be obtained by linear fitting of the related band dispersions vs. the crystal momentum (discussed in Section 2.1). However, in the Dirac cone approximation, the electron band dispersion (E) is determined as [40]:

$$E = \pm v_F |\mathbf{p}| \quad (2)$$

where the \pm sign represents the π^* —upper band and π —lower band, and \mathbf{p} is the crystal momentum denoted as $\mathbf{p} = \hbar(\mathbf{k} - \mathbf{\Gamma K})$ (\hbar is the reduced Planck constant).

In contrast, in GNRs, several (sub)bands (E_n) appear because the quasi-one-dimensional charge carrier confinement in a rectangular (thin) strip whose band structure is described by [41,42]:

$$E_n = \pm \frac{\Delta}{2} \sqrt{n^2 + \frac{2p_{\parallel}^2}{m^* \Delta}} \quad (3)$$

where Δ is the corresponding bandgap, n is the 1D band-index number ($n = 1, 2, 3, \dots$) p_{\parallel} is the parallel wave vector to the direction of the GNR, and m^* remains as the effective electron mass.

It is worth noting that Equation (3) illustrates, at the Γ point in GNRs, a parabolic band dispersion in the eV scale for narrow-width GNRs (e.g., ≤ 10 nm) (Figure S1e) whereas a linear and (quasi) gapless band dispersion is observed for sufficiently wide-width GNRs (e.g., ≥ 100 nm) (Figure S1f). As the ribbon width increases ($w \rightarrow \infty$) the structural conformation and band structure of graphene are recovered. Therefore, wide enough GNRs (Figure S1d) are expected to display graphene-like properties. It is important to note that, in wider GNRs, the effect of the basal plane is more significant than the effect of the edges, while in narrower GNRs, the edges (specifically, whether they are armchair or zigzag edges) are more prominent. In particular, Yang et al. [17] have experimentally shown that the transport properties of graphene are significantly impacted when the ribbon width is ≤ 57 nm. In the present study, we examine systems that are up to eight times wider than this threshold, ensuring the validity of the proposed model.

The bandgap of GNRs can be calculated by using the group velocity of graphene and the ribbon width (w) as the input. The equation for this calculation is given as:

$$\Delta = \frac{2\pi v_F \hbar}{w} \quad (4)$$

Otherwise, the effective electron mass can be determined by using the estimated bandgap and group velocity of graphene, according to the following equation:

$$m^* = \frac{\Delta}{2v_F^2} \quad (5)$$

2.3. Semi-Analytical Model: Describing the Plasmonic Properties

It has been observed experimentally that, in 2D GNR arrays, the plasmon wavelength follows the sample length, which is much larger than the distance between adjacent ribbons and the widths [18]. Interestingly, even though single GNRs can be asymmetric, 2D GNR arrays that are wide enough can be viewed as well-defined 2D planes where the group velocity of graphene can be used to study the plasmonic properties of these systems. With this in mind, the following approach can be used to obtain the plasmon frequency-momentum dispersion [33]:

$$\omega = \text{Re} \left[\sqrt{\frac{2\pi e^2 N_{2D}}{\epsilon m^*} q \cos^2 \theta - \frac{v^2}{4}} - i \frac{v}{2} \right] \quad (6)$$

- e is the well-known electron charge,
- N_{2D} is the 2D electron density,
- ϵ is the dielectric constant,
- q represents the reciprocal wave vector,
- θ represents the plasmon excitation angle,
- v is the electron relaxation rate.

Additionally, if 2D GNR arrays are unsupported (freestanding case) or supported (non-freestanding case), the plasmonic properties can be described by recalculating the effective electron mass (m^*) with the corresponding group velocity of graphene, as reported in [43].

Otherwise, the parameters of Equation (6), i.e., θ , v , and N_{2D} , can be easily manipulated by changing their values or adapting experimentally. From a theoretical notion or experimental side, N_{2D} can also be extracted from the concept of the Fermi level (E_F) [44], as follows:

$$E_F = \hbar v_F \sqrt{2\pi N_{2D}} \quad (7)$$

now, for an intrinsic semiconductor, E_F is found in the middle of the bandgap, i.e., the number of electrons and holes are the same, giving the following expression:

$$E_F = \frac{E_c + E_v}{2} + \frac{k_B T}{2} \ln\left(\frac{N_v}{N_c}\right) \quad (8)$$

where N_c is the effective DOS in the conduction band, N_v is the effective DOS in the valence band, E_c is the conduction band edge, E_v is the valence band edge, k_B is Boltzmann's constant, and T is the absolute temperature.

Hereafter, by the combination of Equations (7) and (8), Equation (6) can be expressed in terms of the needed Fermi level shift as well as the desired temperature. In the present case, we focus only on 2D electron density (N_{2D}) values that are experimentally feasible [33,45]. The equations described so far (Equations (2)–(8)) show a clear dependence on the group velocity of graphene, which cannot be chosen arbitrarily (e.g., $v_F \sim 10^6 \text{ m s}^{-1}$), but must be accurately determined (e.g., by DFT computations as in this work) or measured experimentally.

It is necessary to emphasize that for large values of damping, the radicand in Equation (6) becomes negative, i.e., surface plasmons are absent or shifted to large momenta. Hence, this effect can be understood in terms of the complex (macroscopic) dielectric function [46] denoted as:

$$\epsilon_M(\mathbf{q}, \omega) = \frac{1}{\epsilon^{-1}(\mathbf{q}, \omega)} \quad (9)$$

Equation (9) states that the existence of a plasmon is determined by zeros in the real part of the frequency range where the imaginary part is small or zero. If this condition is not met, only single-particle excitations can be found instead of collective excitations.

2.4. Semi-Analytical Model: Showing the Plasmon Spectrum

Lastly, the plasmon spectrum (the maximum of the plasmon peak) for selected q values can be attained by means of the conventional approach of the spectral line profile using a Lorentzian function, as follows [47]:

$$L = \frac{1}{1 + x^2} \quad (10)$$

where, L is the standard Lorentzian function fixed to a maximum value of 1, and x is an auxiliary (dimensionless) variable denoted as:

$$x = \frac{2(\omega - \omega_0)}{W} \quad (11)$$

here, ω_0 represents the transition frequency of the maximum (THz), ω is the frequency (energy) range of interest, and W is the full width at half maximum (FWHM). The W parameter was set to 0.5 for all spectra unless otherwise stated.

At that point, the plasmon spectrum can be plotted by rearranging Equations (10) and (11) as:

$$L = \frac{1}{1 + \frac{4(\omega - \omega_0)^2}{W^2}} \quad (12)$$

Four important facts should be highlighted:

- (i) Lorentzian line function describes the form of a spectroscopical feature corresponding to a frequency (energy) change in ions, molecules, atoms, or now 2D GNR arrays [48].

- (ii) The units of ω , ω_0 , and W are typically wavenumbers (for absorption spectra) or frequency (for lifetime spectrum of collective excitations) [49]. In the present study, the last entry is used, that is, in terms of frequency, in what we call the plasmon spectrum or maximum of the plasmon peak.
- (iii) The maximum of the plasmon peak could be delayed due to core-electron excitations which are not taken into account in the Lorentzian function [50].
- (iv) The plasmon structure is not expected to be a straightforward Lorentzian peak, but the approach used is useful in clearly showing the control of surface plasmons in 2D GNR arrays.

3. Results and Discussions

3.1. Electronic Properties of Freestanding GNRs

Based on Equation (4) and $v_F = 0.829 \times 10^6 \text{ m s}^{-1}$, Figure 1 shows the bandgap (Δ) as a function of ribbon width ranging from 0.4 to 2.7 nm (ultra-narrow GNRs, Figure 1a) and from 15 to 90 nm (wide GNRs, Figure 1b). The prediction given from 1 to 6 eV by the semi-analytical model (red curve) is in agreement with the predictions of the sophisticated GW approximation for different types of GNRs (3p+1, 3p, and 3p+2) [51]. It is important to keep in mind that the edges (armchair or zigzag edges) of the nanoribbon play a crucial role in determining the bandgap for ultra-narrow GNRs. These edge effects cannot be taken into account explicitly by the simplified model of Equation (4), but the semi-analytical model provides a reasonable prediction for nanoribbons greater than 1 nm, particularly for 3p+1 and 3p families. As mentioned above, edge (atomistic) effects start to be negligible as the ribbon width increases (>60 nm [17]), going from an ultra-confinement on very narrow ribbons to a quasi-confinement on sufficiently wide ribbons. This statement is further confirmed since the bandgap changes dramatically from the eV scale down to a few meV, as discussed below.

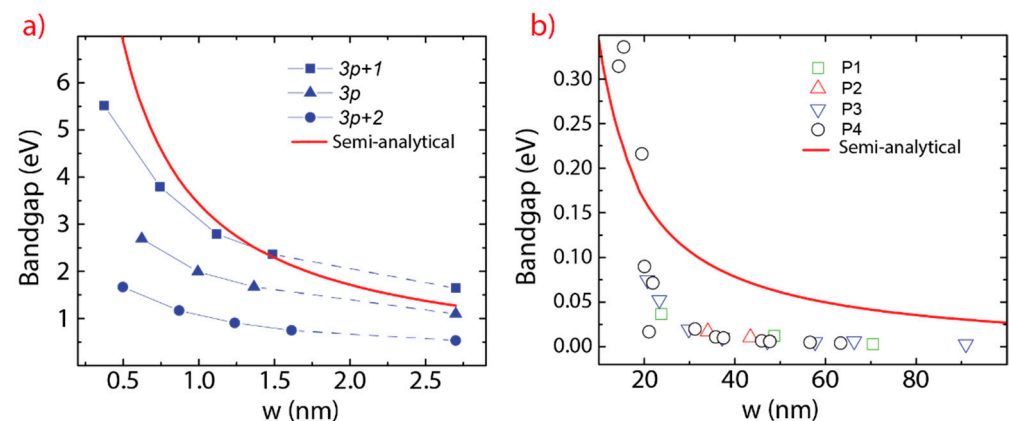


Figure 1. Bandgap vs. the ribbon width. The semi-analytical approach is compared with the results obtained by (a) the GW approximation for diverse types of GNRs and (b) experimental results (P1–P4 denotes different datasets).

Figure 1b compares the prediction of the semi-analytical model (red curve) with the experimental bandgap values (<300 meV) of different GNRs (P1–P4 refers to four different datasets [42]). The predicted bandgaps are consistent across GNRs with widths down to 20 nm. From 20 to 40 nm, the smooth prediction of the semi-analytical model cannot capture the steep dropoff of about 60 meV compared to experiments. Interestingly, the dropoff is reduced to ~25 meV from 40 to 70 nm and as low as 10 meV at 90 nm. While the semi-analytical model may not perfectly match experimental results, it is important to stress that it is not practical to use ab initio methods for electronic properties of wide nanoribbons, as their widths are in the range of tens of nanometers. Additionally, the discrepancy between the model and experiments is expected to be minimal (or non-existent) for experimental

nanoribbons (≥ 155 nm), making the present modeling approach suitable for the GNR systems reported in Ref. [18].

The bandgap of experimental GNRs with widths of 155, 270, 380, and 480 nm are shown in Figure 2 and Table 1. The bandgaps are found to be very small, in the range of a few meV, and the effective electron masses are in agreement with previous studies (Table 1) [42,51]. The semi-analytical model predicts a decrease in bandgap as the ribbon width increases, which is consistent with the experimental results and earlier theoretical reports.

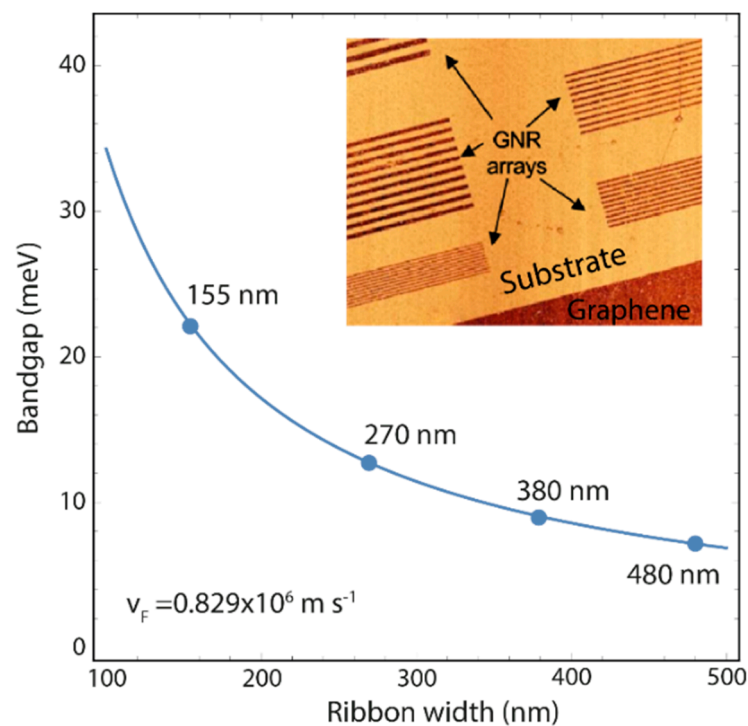


Figure 2. Bandgap vs. the ribbon width of experimental GNRs. The blue line represents a prediction for bandgaps in GNRs with widths ranging from 100 to 500 nm. Figure inset shows 2D periodic arrays of experimental GNRs (adapted with permission of Ref. [18]).

Table 1. Bandgap and electron effective mass of experimental GNRs estimated by the semi-analytical model. The free-electron mass is symbolized as m_0 .

Ribbon Width (nm)	Bandgap (meV)	Effective Mass (m^*) $\times m_0$
155	22.12	2.83×10^{-3}
270	12.70	1.63×10^{-3}
380	9.02	1.16×10^{-3}
480	7.14	0.91×10^{-3}

Figure S3 shows the band structure and DOS of experimental GNRs. The band structure is obtained by applying Equation (3) with the bandgap and effective mass values shown in Table 1. Nine sub-bands ($n = 9$) below/above the Fermi level are introduced, i.e., nine valence and nine conduction sub-bands. It is worth mentioning that the band structure for each graphene nanoribbon is constructed using the same effective mass for all bands. However, when examining plasmonic properties, only the first conduction band and last valence band ($n = 1$) are considered.

The band structure and DOS of the experimental GNRs differ from those of graphene, regardless of the ribbon width. Specifically, a bandgap opening in a few meV is observed at the Γ point, with a parabolic-like band dispersion on a small energy scale and strong peaks in the DOS near the Fermi level. In contrast, graphene has a linear band dispersion at the

K point and no DOS at the Fermi level (Figure S1b,c). In GNRs, this bandgap opening is a direct result of the quasi-one-dimensional confinement of charge carriers, which makes all GNRs semiconducting materials. As stated, the systems under study have very small bandgaps (Table 1), suggesting that they could have plasmonic responses in the terahertz range, which indeed is the range of many photonic and plasmonic applications [52].

Otherwise, the current semiconductor technology requires bandgaps around 1 eV (such as silicon ~ 1.1 eV), in which case, narrow-wide GNRs are the best choice. As an example, using Equation (4), $v_F = 0.829 \times 10^6$ m s $^{-1}$ (freestanding case), and $w = 2.7$ nm (experimentally observed width in GNRs on Ge(001) [53]), the corresponding bandgap is 1.27 eV, slightly above the experimental value (~ 0.9 eV) detected by scanning tunneling spectroscopy (STS) measurements [53].

It is well known that the group velocity of graphene is reduced up to 40% by interacting with germanium or other substrates (non-freestanding case) [15,43]. Keeping this in mind, Figure 3 displays the band structure of experimentally realized GNR on Ge(001) (2.7 nm wide) for different percentage decreases in the group velocity of graphene estimated by LDA-DFT ($v_F = 0.829 \times 10^6$ m s $^{-1}$) (see Table 2). Surprisingly, a perfect agreement between the theoretical and experiment bandgap can be observed at a 30% decrease in the group velocity, i.e., $\Delta_{30\%} = 0.88$ eV.

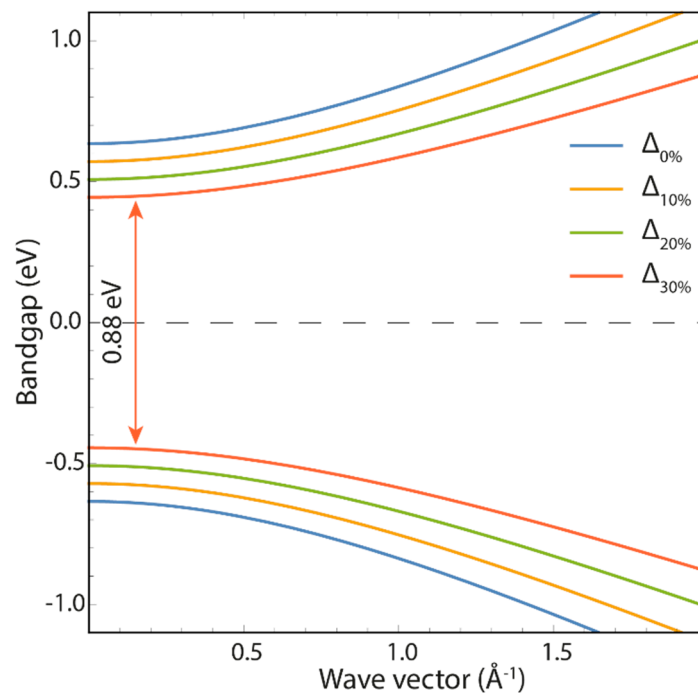


Figure 3. Band structure of experimental realized GNR on Ge(001), considering different percentage decreases (0%, 10%, 20%, 30%) in the group velocity of graphene. The parameters were fixed as: $w = 2.7$ nm and $n = 1$.

Table 2. Bandgap of experimentally realized GNR of 2.7 nm width as a function of the percentage decrease in the group velocity.

v_F	v_F	Bandgap (meV)
0	0.829	1.27
10	0.746	1.14
20	0.663	1.02
30	0.580	0.89
40	0.497	0.76

Furthermore, Ruffieux et al. [54] have reported the fabrication of armchair graphene nanoribbons about 1.5 nm wide on Au(111) with a bandgap of 2.3 eV, an effective electron mass of $0.21 m_0$, and group velocity of $0.82 \times 10^6 \text{ m s}^{-1}$. These results were obtained by angle-resolved photoelectron spectroscopy and scanning tunneling spectroscopy. Interestingly, using the experimental bandgap and ribbon width, the semi-analytical model estimates values practically equal to those observed experimentally ($v_F = 0.809 \times 10^6 \text{ m s}^{-1}$ and $m^* = 0.27m_0$).

The agreement between the experiments and predictions, despite not explicitly taking into account edge effects or other factors (such as passivation, structural disorder, or charge at the edges), confirms that the semi-analytical model is suitable for describing the electronic properties of GNRs.

3.2. Electronic Properties of Non-Freestanding GNRs

As demonstrated, Equation (4) can be used to determine the bandgap of wide nanoribbons on various substrates by changing the substrate and using the corresponding group velocity of graphene, as discussed in the previous section. Indeed, Hwang C. et al., [43] measured the group velocity of graphene on quartz (G/Quartz), hexagonal boron nitride (G/BN), and silicon carbide (G/SiC). Another piece of evidence came from cyclotron mass in graphene device (G/SG) [55], massless relativistic particles (Popov) [33], and LDA-DFT limit (DFT). In this context, we also suggest the growth of experimental (wide) GNRs on this type of substrates, whose predicted bandgap values are shown in Figure 4. Regardless of the substrate, the bandgap values are less than 100 meV and these values decrease as the ribbon gets wider.

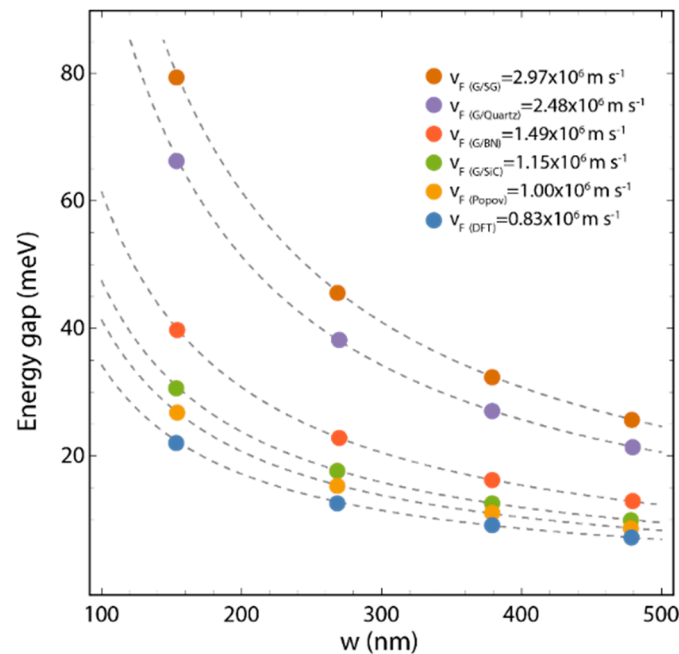


Figure 4. Bandgap variation as a function of the ribbon width. Experimental GNRs ($w = 155, 270, 380, 480 \text{ nm}$) are considered taking into account the group velocity of graphene on various substrates. Dashed curves indicate the bandgap for GNRs from 100 to 500 nm wide.

Interestingly, for high values of v_F , a large bandgap opening is observed, particularly, in GNRs of 155 nm wide. Such bandgap opening corresponds to a 71% increase in quartz, 50% in boron nitride, and 33% in silicon carbide, from the related values predicted by using LDA-DFT computations. Even an increase of 20% is observed compared to the massless relativistic approach. These results constitute the first observation of the dependence on the charge carrier velocity at a fixed ribbon width. This dependence allows achieving, by a

smart choice of supporting substrate, the desired bandgap for a particular application in graphene-based electronic devices.

3.3. Comparison of Semi-Analytical Model with Previous Reports

Before delving into the specific plasmonic properties of the nanoribbons (freestanding and non-freestanding), we first demonstrate the effectiveness of the proposed model by comparing it to previous studies. Unfortunately, there is a lack of experimental evidence for plasmonic properties in the THz frequency range considered here (<50 THz), the 2D GNR arrays under study, and even more importantly in the reciprocal space. To overcome this limitation, we compare the semi-analytical model with more sophisticated modeling approaches, such as TDDFT+RPA (Figure S4) [19] and finite-difference time-domain (FDTD) (Figure 5b) [56], which are commonly used and have demonstrated outstanding agreement between theory and experiment. In addition, the semi-analytical model is tested with results reported for graphene microribbons (Figure 5a) [57].

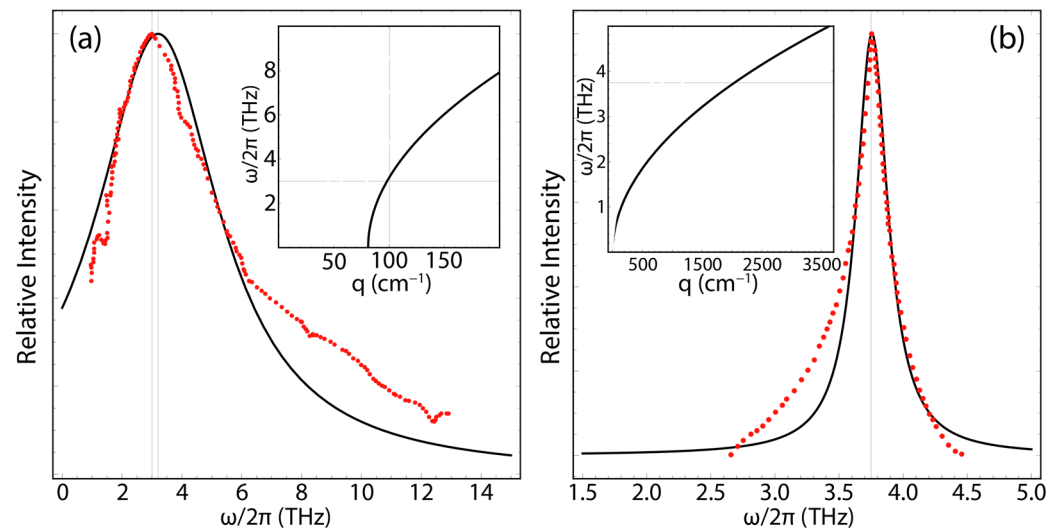


Figure 5. (a) Maximum of the plasmon peak (≤ 15 THz) at momentum $q = 100.6 \text{ cm}^{-1}$. The semi-analytical model (black curve) is compared with the data of Ref. [57] (red points) for graphene microribbon arrays of $4 \mu\text{m}$ wide. Figure inset shows the entire plasmon frequency dispersion up to $q = 200 \text{ cm}^{-1}$. (b) Maximum of the plasmon peak (≤ 5 THz) at momentum $q = 2050 \text{ cm}^{-1}$. The semi-analytical model (black curve) is compared with the predictions of Ref. [56] (red points) for GNR arrays of 10 nm wide. Figure inset shows the entire plasmon frequency dispersion up to $q = 3500 \text{ cm}^{-1}$.

Interestingly enough, Ju et al. [57] have explored the plasmon excitations in engineered graphene microribbon arrays deposited on Si/SiO₂, demonstrating the tunability of plasmon resonances over a broad THz frequency range by changing the ribbon width and electrostatic doping. For example, for one of the scrutinized systems with the following parameters reported: $w = 4 \mu\text{m}$, $q = 100.06 \text{ cm}^{-1}$, $m^* \approx 1.3 \times 10^{-4} m_0$, a doping concentration of $N_{2D} = 1.5 \times 10^{13} \text{ cm}^{-2}$, and electron mobility of $1000 \text{ cm}^{-2}/\text{V s}$ ($\nu = 8.71 \times 10^{13} \text{ s}^{-1}$); the maximum of the plasmon peak is found at 3 THz. The semi-analytical model has accurately reproduced this result with a minor deviation of only 0.20 THz within the frequency range of 1 to 6 THz (Figure 5a, the spectra were normalized by the respective peak values for convenience of comparison). Moreover, the starting plasmon frequency dispersion is shifted to larger values of momenta ($q > 80 \text{ cm}^{-1}$) (see Figure 5a inset).

On the other hand, in Ref. [56], the authors propose the fabrication of 2D arrays of GNRs of 10 nm wide on Si substrates for THz polarizer surface plasmons by using viable conditions such as: $m^* = 0.28 m_0$, $N_{2D} = 4.33 \times 10^{13} \text{ cm}^{-2}$, and assuming the maximum electron mobility ($\nu = 0$). The plasmon response predicted by FDTD was found

in the frequency range from 1.81 to 3.81 THz with the maximum of the plasmon peak at 3.75 THz. By setting these parameters in the semi-analytical model, the plasmon spectrum predicted by the semi-analytical model is found in excellent agreement at $q = 2050 \text{ cm}^{-2}$ (Figure 5b, the spectra were normalized using the corresponding maximum values to facilitate comparison). Forbidden plasmon regions are absent in the plasmon frequency dispersion (Figure 5b inset).

From the ab initio side, in Ref. [19], the authors reported that freestanding and narrow armchair GNRs arranged as 2D periodic arrays have an effective electron mass of $0.36m_0$. By directly establishing this value in Equation (6), which in fact is independent of the group velocity of graphene at that point, a perfect agreement between both approaches can be observed in the plasmon frequency-momentum dispersion for a change in the Fermi level (doping) of up to 0.3 eV ($N_{2D} = 3.67 \times 10^{12} \text{ cm}^{-2}$, orange curve). For higher values of doping (0.4 eV, purple line), a discrepancy is observed. All these results allow us to demonstrate the reliability of the semi-analytical model and can be used to describe the plasmonic properties of 2D GNR arrays of interest.

A final remark, while the semi-analytical model accurately predicts the experimental results, it is important to note two important facts: (i) in practice, the non-freestanding GNRs will be supported by two anchors and may vibrate mechanically, altering their phonon structure, and (ii) nearby materials could affect the electric or magnetic fields generated. Hence, the simplified model does not take into account these factors, so caution should be taken during experiments to avoid inconsistencies. This can be achieved through proper gating voltage selection or adjusting the electric field applied to ω , which is given as $E(\omega) = E_0 \exp(-i\omega t)$.

3.4. Plasmonic Properties of Non-Freestanding GNRs

Now, Figure 6 shows the plasmon frequency-momentum dispersions of 2D GNR arrays from 155 to 480 nm and subject to different group velocities. The parameter of Equation (6) ($N_{2D} = 1.0 \times 10^{12} \text{ cm}^{-2}$, $v = 1.0 \times 10^{13} \text{ s}^{-1}$, and $\theta = 0$) have been fixed based on experimentally feasible values [33,45]. As observed, the plasmon trends follow a \sqrt{q} -like dispersion from 0 to $10,000 \text{ cm}^{-1}$. This plasmon dispersion is characteristic of 2D materials [55]. More importantly, by increasing the value of v_F , the plasmon frequency increases.

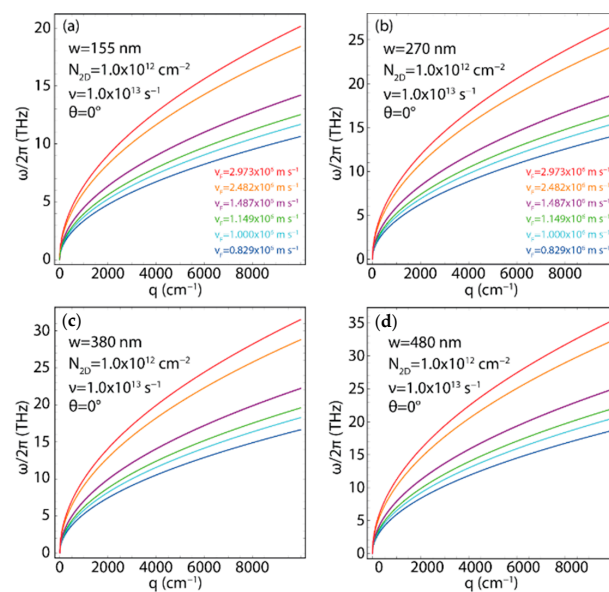


Figure 6. Frequency–momentum dispersion as a function of the plasmon momentum, considering the group velocity of graphene on various substrates for 2D GNR arrays of (a) $w = 155 \text{ nm}$, (b) $w = 270 \text{ nm}$, (c) $w = 380 \text{ nm}$, (d) $w = 480 \text{ nm}$.

For an illustrative example, at the end of the sampled momentum ($q = 10,000 \text{ cm}^{-1}$), an increase of ~ 9 THz is observed for 2D GNR arrays of 155 nm wide (Figure 6a), considering the group velocity of graphene obtained by LDA-DFT computations ($v_F = 0.829 \times 10^6 \text{ m s}^{-1}$, blue curve) and that obtained from graphene on quartz ($v_F = 2.482 \times 10^6 \text{ m s}^{-1}$, orange curve). Similarly, an increase of almost 13 THz is detected for 2D GNR arrays of 270 nm wide (Figure 6b), 16 THz for 2D GNR arrays of 380 nm wide (Figure 6c), and 20 THz for 2D GNR arrays of 480 nm wide (Figure 7d).

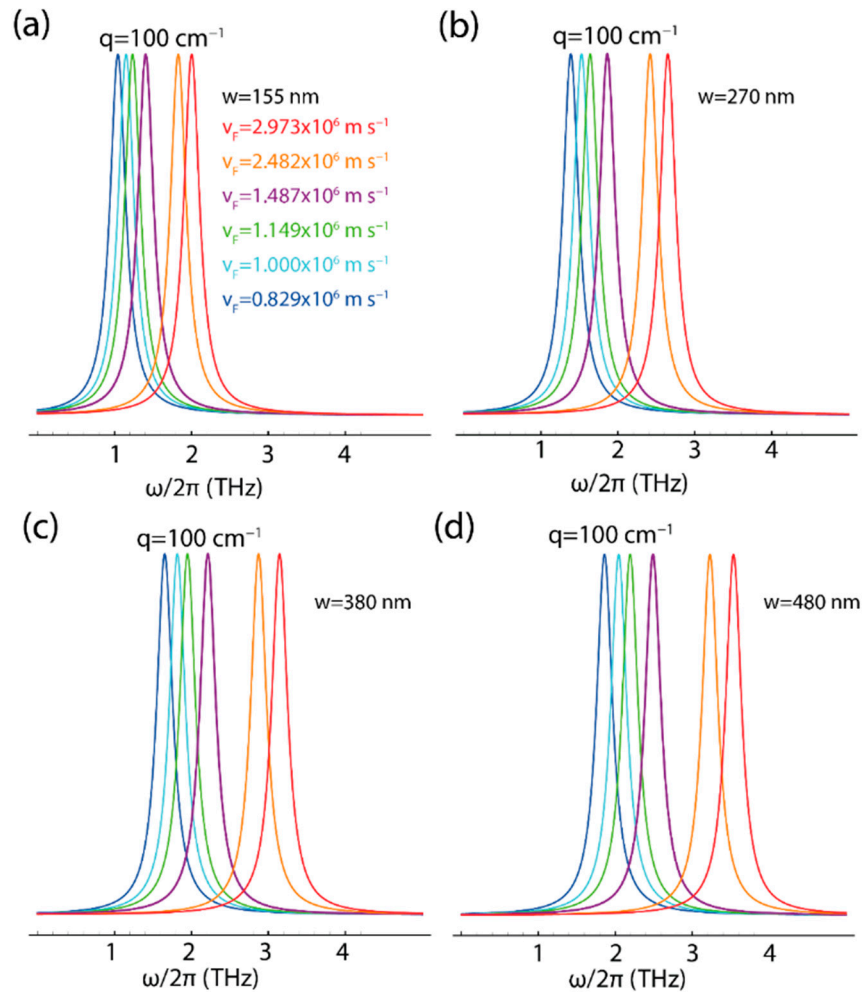


Figure 7. Maximum of the plasmon peak (≤ 5 THz) at plasmon momentum $q = 100 \text{ cm}^{-1}$, considering the group velocity of graphene onto various substrates for 2D GNR arrays of (a) $w = 155 \text{ nm}$, (b) $w = 270 \text{ nm}$, (c) $w = 380 \text{ nm}$, (d) $w = 480 \text{ nm}$.

By implementing Equation (12) at $q = 100 \text{ cm}^{-1}$, Figure 7 demonstrates the controllability and tunability of the plasmon response of 2D GNR arrays by varying the group velocity of graphene as well as the ribbon width: $w = 155 \text{ nm}$ (Figure 7a), $w = 270 \text{ nm}$ (Figure 7b), $w = 380 \text{ nm}$ (Figure 7c), and $w = 480 \text{ nm}$ (Figure 7d). Interestingly, it can be seen that keeping momentum fixed (i.e., $q = 100 \text{ cm}^{-1}$) while varying the ribbon width and the charge carrier velocity, the maximum of the plasmon peak is found at higher frequencies, suggesting that the effect of group velocity is more critical in wider nanoribbons. To clarify this fact, for $w = 155 \text{ nm}$ and freestanding cases (blue curves), the maximum of the peak is almost at 0.9 THz (Figure 7a) while for $w = 480 \text{ nm}$, the maximum of the peak is observed at almost 1.4 THz (Figure 7d). On the contrary, for graphene on quartz (orange curves), the maximum of the plasmon peak is observed at almost 2 THz (Figure 7a) for $w = 155 \text{ nm}$, and at almost 3.5 THz for $w = 480 \text{ nm}$ (Figure 7d). From these results, it is

noticed a percentage variation of up to 35% and 43% in the position of the maximum of the plasmon peak, in each case respectively.

3.5. Plasmonic Properties of Freestanding GNRs: The Effect of Ribbon Width (w)

The results discussed in the previous sections allow us to understand the versatility of 2D periodic arrangements of GNRs (i.e., 2D GNR arrays) by changing the supporting substrate and ribbon width, which can be exploited in the design of novel nanophotonic devices.

In what follows in the article, we focus on the freestanding cases and parameters such as 2D electron concentration (doping) (N_{2D}). While the parameters of Equation (6) can be varied trivially, the goal is to be able to use this simple model with parameters that can be fixed and measured in experiments. In this context:

- The manipulation of the plasmon excitation angle (θ) in 2D GNR arrays is imperative to obtain the surface plasmon resonance and the related sensitivity. However, Equation (6) must be used with caution since, at $\theta = 90$, the radicand becomes zero. More importantly, the properties and features of oblique plasmons can be scrutinized.
- In conductivity-related phenomena, charge carrier mobility plays an important role in the electronic and plasmonics properties of any system. Thus, high-charge carrier mobility is commonly observed in defect-free graphene samples, whereas charge carrier mobility is significantly reduced in graphene samples with high concentrations of defects. From the experimental part, this effect depends on the synthesis process. From the theoretical part, in Equation (6), this fact is introduced by the electron relaxation rate (ν), taking into account the following statement: a high value of ν is connected with a low charge carrier mobility, and vice-versa.
- 2D electron concentration (N_{2D}) (or 2D charge carrier density) can be controlled by injecting or ejecting electrons, i.e., by either doping the GNR system or by gating voltages. The latter technique is of particular interest because it can be varied in a reasonable range up to $N_{2D} = 5.0 \times 10^{12} \text{ cm}^{-2}$ [42].

Before discussing the effect of the 2D electron concentration (Section 3.6), we probe a little into the effect of ribbon width in freestanding cases. Figure S5a displays the plasmon frequency–momentum dispersion of 2D GNR arrays for $w = 155 \text{ nm}$ (blue curve), $w = 270 \text{ nm}$ (cyan curve), $w = 380 \text{ nm}$ (green curve), and $w = 480 \text{ nm}$ (red curve). Again, the important fact is the increase in the plasmon frequency with increasing ribbon width. To further evidence the tunability of plasmon response, Figure S5b shows the maximum of the plasmon peak at $q = 1000 \text{ cm}^{-1}$. Specifically, the peak position is found at 3.35 THz for $w = 155 \text{ nm}$, at 4.34 THz for $w = 270 \text{ nm}$, at 5.26 THz for $w = 380 \text{ nm}$, and at 5.91 THz for $w = 480 \text{ nm}$.

Figure S5c shows the percentage variation in plasmon frequency for three different testing momenta ($q = 100, 1000, 10,000 \text{ cm}^{-1}$). Although it is observed that increasing the ribbon width also increases the plasmon frequency, it can be noted that this effect is independent of momentum, resulting in a constant trend in plasmon frequency rate in all cases, that is, ~25% from 155 to 270 nm, ~16% from 270 to 380 nm, and ~11% from 380 to 480 nm. A close view of Figure S5c shows a slight variation at 100 (black marker), 1000 (red marker), and 10,000 (blue marker) cm^{-1} , because the width increment from 155 to 270 nm results in a percentage variation of 25.36%, 24.38%, and 26.16%, respectively. Additionally, it can be noticed that the plasmon frequency rate can be described with a decreasing exponential function, which suggests that as the ribbon width increases, the effect on the plasmon frequency dispersion is gradually minor. The decreasing behavior of the plasmon frequency rate can be corroborated by inspecting more values of q .

3.6. Plasmonic Properties of Freestanding GNRs: The Effect of 2D Charge Density (N_{2D})

The parameters in Equation (6) can be easily adjusted by any researcher, but the goal is to use the model with experimental results or those obtained from more advanced predictions (such as TDDFT + RPA [19] and FDTD [56]). This study aims to provide a

practical guide for describing the sensitivity and detection of surface plasmons in real-world situations, at least in rough approximation.

Based on the measurements of Ref. [45], three different 2D charge carrier concentrations are used ($N_{2D} = 1.0 \times 10^{12} \text{ cm}^{-2}$, $N_{2D} = 2.0 \times 10^{12} \text{ cm}^{-2}$, and $N_{2D} = 4.0 \times 10^{12} \text{ cm}^{-2}$) (Figure 8a–d). Regardless of the ribbon width, increasing the value of N_{2D} also significantly increases the plasmon frequency. This plasmon frequency increases by up to almost 40 THz (Figure 8d) which is much greater than that observed if only the ribbon width is increased (Figure S5a), i.e., approximately twice in magnitude. The entire frequency-momentum dispersion is below 21 THz for $w = 155 \text{ nm}$ (Figure 8a), 27 THz for $w = 270 \text{ nm}$ (Figure 8b), 33 THz for $w = 380 \text{ nm}$ (Figure 8c), and 40 THz for $w = 480 \text{ nm}$ (Figure 8d). Note that the largest increase in plasmon frequency is achieved at $N_{2D} = 4.0 \times 10^{12} \text{ cm}^{-2}$ (red curves). It is also detected that the plasmon dispersion starts at zero frequency and zero momentum, that is, forbidden plasmon regions are unexpected to occur. If the plasmon response needs to be shifted to large values of q , high values of plasmon excitation angle or electron relaxation rate can be introduced (separately or combined) in Equation (6), for instance, at $\theta = 80$ and $\nu = 4.0 \times 10^{13} \text{ s}^{-1}$.

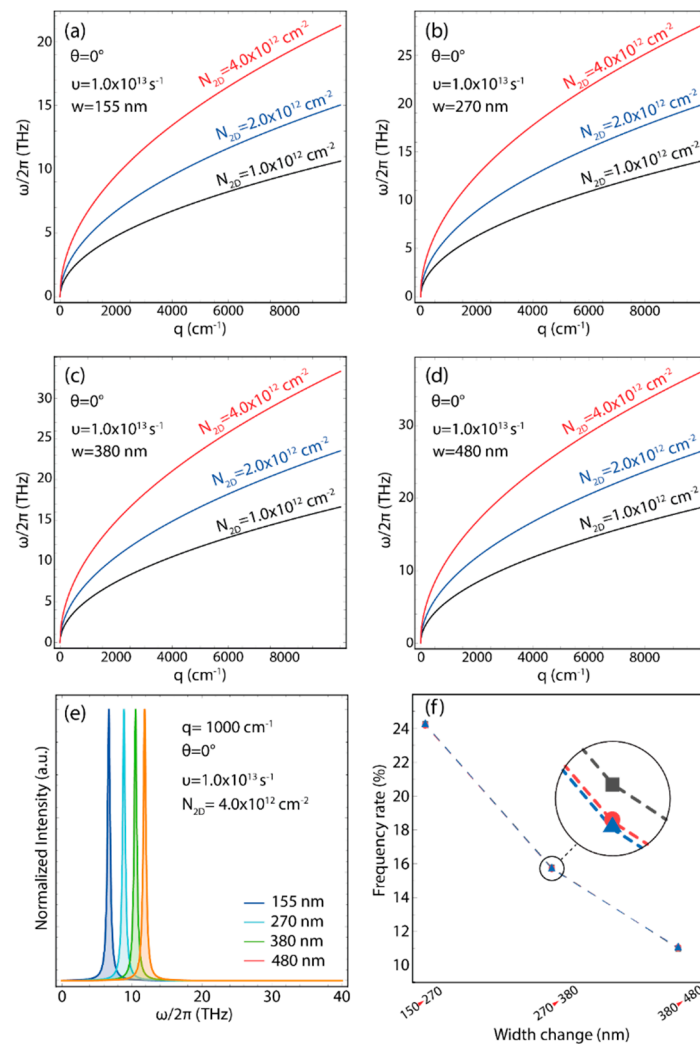


Figure 8. Frequency–momentum dispersion as a function of the plasmon momentum using the charge carrier velocity of freestanding graphene ($v_F = 0.829 \times 10^6 \text{ m s}^{-1}$) for the experimental 2D GNR arrays of (a) $w = 155 \text{ nm}$, (b) $w = 270 \text{ nm}$, (c) $w = 380 \text{ nm}$, (d) $w = 480 \text{ nm}$. (e) Maximum of the plasmon peak ($\leq 40 \text{ THz}$) at plasmon momentum $q = 1000 \text{ cm}^{-1}$, considering different ribbon widths. (f) Percentage variation in plasmon frequency rate as a function of the ribbon width increment, for three selected plasmon momenta ($q = 1000, 5000, 10,000 \text{ cm}^{-1}$).

Figure 8e clearly shows the controllability and tunability of the maximum of the plasmon peak for a fixed momentum ($q = 1000 \text{ cm}^{-1}$) and at the highest value of 2D charge carrier concentration ($N_{2D} = 4.0 \times 10^{12} \text{ cm}^{-2}$). The maximum is found at 6.72 THz for $w = 155 \text{ nm}$ (blue curve), at 8.87 THz for $w = 270 \text{ nm}$ (cyan curve), at 10.53 THz for $w = 380 \text{ nm}$ (green curve), and at 11.83 THz for $w = 480 \text{ nm}$ (orange curve). In general, the plasmon frequency end is detected at 21.26 THz ($w = 155 \text{ nm}$), 28.06 THz ($w = 270 \text{ nm}$), 33.29 THz ($w = 380 \text{ nm}$), and 37.42 THz ($w = 480 \text{ nm}$). These results fall below the limit of the semi-analytical model used here and are anticipated to match future experimental findings.

Figure 8f shows that the plasmon frequency rate is not affected by the variation of the ribbon width for testing momenta ($q = 1000, 5000, 10,000 \text{ cm}^{-1}$). As result, one can note a constant trend in the plasmon frequency rate in all cases, that is, $\sim 24\%$ from 155 to 270 nm, $\sim 16\%$ from 270 to 380 nm, and $\sim 11\%$ from 380 to 480 nm. Additionally, it has been confirmed that the plasmon frequency rate can be represented by a decreasing exponential function, indicating that as the ribbon width increases, its impact on the plasmon frequency dispersion becomes progressively smaller.

4. Chlorpyrifos-Methyl Sensing

We now explore the potential application of 2D GNR arrays in molecular sensing (Figures 9 and 10 and Table 3). Chlorpyrifos-methyl is an insecticide that is widely used to control insect pests on various crops, but it is highly toxic to organisms and humans. When exposed to it, negative impacts on the nervous system can occur, including headaches, dizziness, and nausea. Research has connected chlorpyrifos-methyl to developmental problems in children, such as decreased IQ and attention deficit disorders. Given these concerns, numerous nations have taken action to restrict or prohibit the utilization of chlorpyrifos-methyl [58,59]. Therefore, effective detection and removal methods are crucial. From a chemical perspective, chlorpyrifos-methyl has a benzene ring with perpendicular π electrons that are likely to interact directly with the perpendicular π electrons of the GNRs via $\pi - \pi$ interactions. Additionally, this molecule has a resonance plasmon peak at 0.95 THz [60]. These types of molecules are often detected in water [59], but water has a strong THz absorption at 1 THz [61]. In this context, materials with resonance peaks within the range of water frequency absorption significantly enhance the interaction between incident THz waves and target molecules, making them useful for sensing proteins, nucleic acids, and cells.

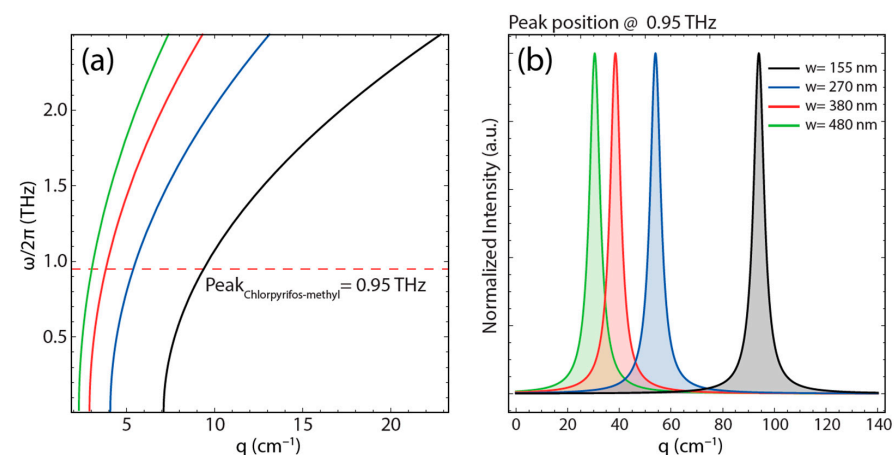


Figure 9. (a) Frequency–momentum dispersion as a function of the plasmon momentum using the charge carrier velocity of freestanding graphene ($v_F = 0.829 \times 10^6 \text{ m s}^{-1}$) for the experimental 2D GNR arrays ($w = 155, 270, 380, 480 \text{ nm}$). (b) Maximum of the plasmon peak at 0.95 THz as a function of the plasmon momentum for the same systems.

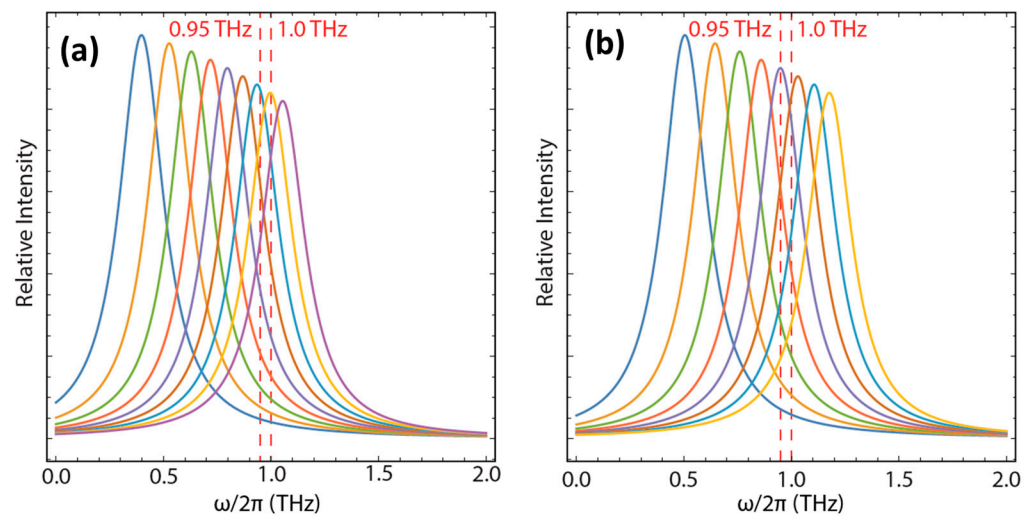


Figure 10. Dispersion of the maximum of the plasmon peak (<2 THz) with FWHM = 5 for (a) $w = 155$ nm by considering different momenta from 75 (blue curve) to 100 cm^{-1} (purple curve), and (b) $w = 480$ nm by considering different momenta from 25 (blue curve) to 35 cm^{-1} (orange curve).

Table 3. Position of the maximum of the plasmon peak at 0.95 THz for the experimental 2D GNR arrays analyzed.

Ribbon Width (nm)	Peak Position (cm^{-1})
155	94.2
270	54.1
380	38.5
480	30.5

Figure 9a shows that 2D GNR arrays can effectively serve as a sensing platform for detecting chlorpyrifos-methyl molecules by using a specific setting, for example: $N_{2D} = 2.5 \times 10^{12}\text{ cm}^{-2}$, $\theta = 0$, and $\nu = 2.24\text{ s}^{-1}$. All the analyzed cases ($w = 155$ nm, black curve; $w = 270$ nm, blue curve; $w = 380$ nm, red curve; $w = 480$ nm, green curve) have the necessary THz response. It is worth noting that high values of the electron relaxation rate (ν) and charge carrier concentration (N_{2D}) are used, which implies two important facts:

- (i) The use of $\nu = 2.24\text{ s}^{-1}$ is justified by the possibility of using GNRs with a high concentration of defects, such as oxidized graphene ribbons [62].
- (ii) It is assumed that the interaction between the 2D GNR array and the chlorpyrifos-methyl molecule through $\pi - \pi$ interactions will cause a transfer of charge (doping) from the molecule, which validate the use of $N_{2D} = 2.5 \times 10^{12}\text{ cm}^{-2}$.

Additionally, in Figure 9a, small forbidden plasmon regions are detected at $q < 80\text{ cm}^{-1}$ for $w = 155$ nm and at $q < 40\text{ cm}^{-1}$ for $w = 270$ nm. In the remaining two cases ($w = 380$ nm and $w = 480$ nm), the forbidden regions appear at $q < 20\text{ cm}^{-1}$. Thus, as the ribbon width increases, the momentum range for which the plasmon does not exist shrinks, indicating that for $w \rightarrow \infty$, the plasmon dispersion resembles the results of 2D graphene (i.e., THz = 0 and $q = 0$). Additionally, the plasmon frequency dispersion increases as the ribbon width increases, reaching nearly 6 THz at $q = 300\text{ cm}^{-1}$ and $w = 480$ nm (green curve, Figure S6). Importantly, Figure 9b shows that while all 2D GNR arrays have plasmon responses at 0.95 THz, these resonance modes shift to lower values of q as the ribbon width increases. The same shift has been observed in experimental graphene microribbons ranging from 1 to $4\text{ }\mu\text{m}$ [57]. For example, in Table 3, for $w = 155$ nm, the peak position at 0.95 THz is at $q \approx 94\text{ cm}^{-1}$ (black curve) whereas for $w = 480$ nm the peak position is at $q \approx 30\text{ cm}^{-1}$ (green curve). Using 2D GNR arrays with a larger range of ribbon widths, THz resonance from 0.1–1 THz can be straightforwardly engineered.

Subsequently, Figure 10 depicts the presence of plasmon resonances in 2D GNR arrays with widths of 155 nm (Figure 10a) and 480 nm (Figure 10b), respectively. These resonance modes are found in the same frequency of water (1 THz) at $q \approx 99 \text{ cm}^{-1}$ for $w = 155 \text{ nm}$ (orange curve) and $q \approx 30 \text{ cm}^{-1}$ for $w = 480 \text{ nm}$ (brown curve). In the context of plasmonic–organic molecule interactions, it is worth mentioning that the interaction between the plasmonic wave and organic molecules can cause changes in the signal that is generated. In particular, this interaction can cause changes in the resonance frequency of the plasmon modes detected in the analyzed 2D GNR arrays, leading to modifications in the optical signal observed here (for water or chlorpyrifos-methyl). The precise nature of these signal modifications depends on the specific details of the interaction between the plasmonic wave and the organic molecule, further including the size and shape of the molecule, its electrical properties, and its position relative to the incident plasmon wave. Understanding these interactions is an important area of plasmonics research and has immediate applications in fields such as biosensing, photonics, and optoelectronics as well as the design of novel graphene-based biosensors.

5. Conclusions

In summary, we used a semi-analytical approach, which takes into account the Dirac cone approximation and the group velocity of graphene ($v_F = 0.829 \times 10^6 \text{ m s}^{-1}$) to examine the electronic and plasmonic features of GNRs with widths that match those of actual samples (155, 270, 380, and 480 nm). Both freestanding and non-freestanding models were considered. The band structure and bandgap were evaluated in the range of a few meV to eV. Plasmon resonances were evaluated in the frequency range below 50 THz.

From the viewpoint of electronic properties, this modeling approach reasonably reproduces the bandgaps of experimental samples (>20 nm wide) and values predicted by sophisticated GW approximation (with widths from 1.5 to 2.7 nm). Moreover, it is possible to match the experimental bandgap (~0.9 eV) of GNRs (10 nm wide) on Ge(001) at a 30% decrease in the group velocity of graphene estimated by LDA-DFT computations as well as the effective electron mass ($m^* = 0.27m_0$) of GNRs (~1 nm wide) on Au(111). With this evidence, this work demonstrated that the bandgaps of the systems under examination ($\geq 155 \text{ nm}$) range from 7 to 22 meV. These bandgaps values can be increased by increasing the group velocity of graphene when it is supported on various substrates such as quartz, and hexagonal boron nitride, among others.

Considering the plasmonics side, this work is restricted to the analysis of the effect of changing the group velocity of graphene, ribbon width, and charge carrier concentration (doping). Other parameters such as plasmon excitation angle, electron mobility, temperature, and Fermi level shift can be scrutinized by simple modification of these values in Equation (6). Specifically, the semi-analytical model reproduced the experiment of graphene microribbons of 4 μm wide organized as 2D periodic arrays, finding the maximum of the plasmon peak at 3.20 THz for $q = 100.06 \text{ cm}^{-1}$ as well as the predictions of GNRs of 10 nm wide on Si with the maximum of the plasmon peak at 3.75 THz for $q = 2050 \text{ cm}^{-1}$. For the systems under study, the plasmon frequency dispersion rises as the group velocity of graphene increases. The plasmon frequency further increases by increasing the ribbon width or the charge carrier concentration up to about 50 THz for $q = 10,000 \text{ cm}^{-1}$. The decay of the plasmon frequency rate suggested that as the ribbon width grows, the effect on the plasmon frequency dispersion became gradually minor.

The potential application of the systems considered was discussed in terms of molecular sensing of chlorpyrifos-methyl, which is a highly toxic pesticide for organisms and humans. By setting the following parameters: $N_{2D} = 2.5 \times 10^{12} \text{ cm}^{-2}$, $\theta = 0$, and $v = 2.24 \text{ s}^{-1}$, all the analyzed cases displayed plasmons resonances at the same frequency of chlorpyrifos-methyl (0.95 THz) and water (1 THz), suggesting that 2D GNR arrays are excellent platforms for the design of novel biosensing devices.

Although this modeling approach has some restrictions, such as its frequency range of use and its failure to explicitly consider the effects of sample passivation, ribbon edges, and

disorder, it still demonstrates good agreement with previous experiments and predictions. This semi-analytical model is therefore useful as a preliminary step in determining the theoretical electronic and plasmonic properties of viable samples of graphene or graphene-related ribbons.

Supplementary Materials: The following supporting information can be downloaded at: <https://www.mdpi.com/article/10.3390/cryst13020311/s1>. Figures S1–S6.

Author Contributions: Conceptualization, T.T. and C.V.G.; Methodology, N.B.G., M.B. and C.V.G.; Validation, T.T., M.G. and C.V.G.; Formal Analysis, C.V.G.; Resources, T.T.; Data Curation, T.T.; Writing—Original Draft Preparation, C.V.G.; Writing—Review & Editing, C.V.G.; Visualization, M.G.; Project Administration, T.T.; Funding Acquisition, T.T. All authors have read and agreed to the published version of the manuscript.

Funding: This work was supported by Universidad Técnica Particular de Loja (UTPL-Ecuador) (RUC No. 1190068729001).

Acknowledgments: T.T., M.G. and C.V.G. wish to thank the Ecuadorian National Department of Sciences and Technology (SENESCYT).

Conflicts of Interest: The authors declare no conflict of interest.

References

1. Abergel, D.; Apalkov, V.; Berashevich, J.; Ziegler, K.; Chakraborty, T. Properties of graphene: A theoretical perspective. *Adv. Phys.* **2010**, *59*, 261–482. [[CrossRef](#)]
2. Castro, A.H.; Guinea, F.; Peres, N.M.R.; Novoselov, K.S.; Geim, A.K. The electronic properties of graphene. *Rev. Mod. Phys.* **2009**, *81*, 109. [[CrossRef](#)]
3. Celis, A.; Nair, M.N.; Taleb-Ibrahimi, A.; Conrad, E.H.; Berger, C.; de Heer, W.A.; Tejeda, A. Graphene nanoribbons: Fabrication, properties and devices. *J. Phys. D Appl. Phys.* **2016**, *49*, 143001. [[CrossRef](#)]
4. Novoselov, K.S.; Geim, A.K.; Morozov, S.V.; Jiang, D.; Zhang, Y.; Dubonos, S.V.; Grigorieva, I.V.; Firsov, A.A. Electric field effect in atomically thin carbon films. *Science* **2004**, *306*, 666–669. [[CrossRef](#)] [[PubMed](#)]
5. Wu, J.; Lin, H.; Moss, D.J.; Loh, K.P.; Jia, B. Graphene oxide for photonics, electronics and optoelectronics. *Nat. Rev. Chem.* **2023**, 1–22. [[CrossRef](#)]
6. Kim, K.; Choi, J.-Y.; Kim, T.; Cho, S.-H.; Chung, H.-J. A role for graphene in silicon-based semiconductor devices. *Nature* **2011**, *479*, 338–344. [[CrossRef](#)] [[PubMed](#)]
7. Kamedulski, P.; Lukaszewicz, J.; Witczak, L.; Szroeder, P.; Ziolkowski, P. The Importance of Structural Factors for the Electrochemical Performance of Graphene/Carbon Nanotube/Melamine Powders towards the Catalytic Activity of Oxygen Reduction Reaction. *Materials* **2021**, *14*, 2448. [[CrossRef](#)] [[PubMed](#)]
8. González, Z.; Acevedo, B.; Predeanu, G.; Axinte, S.M.; Drăgoescu, M.-F.; Slăvescu, V.; Fernandez, J.J.; Granda, M.; Gryglewicz, G.; Melendi-Espina, S. Graphene materials from microwave-derived carbon precursors. *Fuel Process. Technol.* **2021**, *217*, 106803. [[CrossRef](#)]
9. Tene, T.; Arias, F.A.; Guevara, M.; Nuñez, A.; Villamagua, L.; Tapia, C.; Pizarra, M.; Torres, F.J.; Caputi, L.S.; Gomez, C.V. Removal of mercury(II) from aqueous solution by partially reduced graphene oxide. *Sci. Rep.* **2022**, *12*, 6326. [[CrossRef](#)]
10. Pereira, P.; Ferreira, D.P.; Araújo, J.C.; Ferreira, A.; Fanguero, R. The Potential of Graphene Nanoplatelets in the Development of Smart and Multifunctional Ecomposites. *Polymers* **2020**, *12*, 2189. [[CrossRef](#)] [[PubMed](#)]
11. Li, X.; Shen, Q.; Zhang, Y.; Wang, L.; Nie, C. Wear behavior of electrodeposited nickel/graphene composite coating. *Diam. Relat. Mater.* **2021**, *119*, 108589. [[CrossRef](#)]
12. Tseluikin, V.; Zhang, L. Carbon and Carbon-Based Composite Thin Films/Coatings: Synthesis, Properties and Applications. *Coatings* **2022**, *12*, 907. [[CrossRef](#)]
13. Sahoo, S.; Bhuyan, M.; Sahoo, D. Tuning of dielectric and magnetic performance of graphene oxide via defect regulation by metal oxide nanoparticle for high temperature device. *J. Alloy. Compd.* **2023**, *935*, 168097. [[CrossRef](#)]
14. Dong, X.; Huang, W.; Chen, P. In Situ Synthesis of Reduced Graphene Oxide and Gold Nanocomposites for Nanoelectronics and Biosensing. *Nanoscale Res. Lett.* **2011**, *6*, 1–6. [[CrossRef](#)]
15. Kim, H.W.; Ko, W.; Joo, W.-J.; Cho, Y.; Oh, Y.; Ku, J.; Jeon, I.; Park, S.; Hwang, S.W. Unraveling the Structural and Electronic Properties of Graphene/Ge(110). *J. Phys. Chem. Lett.* **2018**, *9*, 7059–7063. [[CrossRef](#)] [[PubMed](#)]
16. Tian, C.; Miao, W.; Zhao, L.; Wang, J. Graphene nanoribbons: Current status and challenges as quasi-one-dimensional nanomaterials. *Rev. Phys.* **2023**, *10*, 100082. [[CrossRef](#)]
17. Yang, Y.; Murali, R. Impact of Size Effect on Graphene Nanoribbon Transport. *IEEE Electron Device Lett.* **2010**, *31*, 237–239. [[CrossRef](#)]

18. Fei, Z.; Goldflam, M.D.; Wu, J.-S.; Dai, S.; Wagner, M.; McLeod, A.S.; Liu, M.K.; Post, K.W.; Zhu, S.; Janssen, G.C.A.M.; et al. Edge and Surface Plasmons in Graphene Nanoribbons. *Nano Lett.* **2015**, *15*, 8271–8276. [[CrossRef](#)]
19. Gomez, C.V.; Pisarra, M.; Gravina, M.; Pitarke, J.M.; Sindona, A. Plasmon Modes of Graphene Nanoribbons with Periodic Planar Arrangements. *Phys. Rev. Lett.* **2016**, *117*, 116801. [[CrossRef](#)]
20. Yin, H.; Zhang, H. Plasmons in graphene nanostructures. *J. Appl. Phys.* **2012**, *111*, 103502. [[CrossRef](#)]
21. Mousavi, S.T.; Badehian, H.A.; Gharbavi, K. Optical spectra of zigzag graphene nanoribbons: A first-principles study. *Phys. Scr.* **2022**, *97*, 105803. [[CrossRef](#)]
22. Toudert, J.; Serna, R. Interband transitions in semi-metals, semiconductors, and topological insulators: A new driving force for plasmonics and nanophotonics [Invited]. *Opt. Mater. Express* **2017**, *7*, 2299–2325. [[CrossRef](#)]
23. Gan, C.H.; Gbur, G.; Visser, T.D. Surface Plasmons Modulate the Spatial Coherence of Light in Young’s Interference Experiment. *Phys. Rev. Lett.* **2007**, *98*, 043908. [[CrossRef](#)] [[PubMed](#)]
24. Low, T.; Avouris, P. Graphene Plasmonics for Terahertz to Mid-Infrared Applications. *ACS Nano* **2014**, *8*, 1086–1101. [[CrossRef](#)] [[PubMed](#)]
25. Wu, L.; Chu, H.S.; Koh, W.S.; Li, E.P. Highly sensitive graphene biosensors based on surface plasmon resonance. *Opt. Express* **2010**, *18*, 14395–14400. [[CrossRef](#)]
26. Fu, H.; Zhang, S.; Chen, H.; Weng, J. Graphene Enhances the Sensitivity of Fiber-Optic Surface Plasmon Resonance Biosensor. *IEEE Sens. J.* **2015**, *15*, 5478–5482. [[CrossRef](#)]
27. Sadeghi, Z.; Shirvani, H. Highly sensitive mid-infrared SPR biosensor for a wide range of biomolecules and biological cells based on graphene-gold grating. *Phys. E. Low-dimensional Syst. Nanostructures* **2020**, *119*, 114005. [[CrossRef](#)]
28. Zhang, H.; Song, D.; Gao, S.; Zhang, J.; Zhang, H.; Sun, Y. Novel SPR biosensors based on metal nanoparticles decorated with graphene for immunoassay. *Sens. Actuators B Chem.* **2013**, *188*, 548–554. [[CrossRef](#)]
29. Mulpur, P.; Podila, R.; Lingam, K.; Vemula, S.K.; Ramamurthy, S.S.; Kamiseti, V.; Rao, A.M. Amplification of Surface Plasmon Coupled Emission from Graphene–Ag Hybrid Films. *J. Phys. Chem. C.* **2013**, *117*, 17205–17210. [[CrossRef](#)]
30. Ling, X.; Xie, L.; Fang, Y.; Xu, H.; Zhang, H.; Kong, J.; Dresselhaus, M.S.; Zhang, J.; Liu, Z. Can Graphene Be Used as a Substrate for Raman Enhancement? *Nano Lett.* **2010**, *10*, 553–561. [[CrossRef](#)]
31. Pisarra, M.; Gomez, C.V.; Sindona, A. Massive and massless plasmons in germanene nanosheets. *Sci. Rep.* **2022**, *12*, 18624. [[CrossRef](#)] [[PubMed](#)]
32. Sindona, A.; Gomez, C.V.; Pisarra, M. Dielectric screening versus geometry deformation in two-dimensional allotropes of silicon and germanium. *Sci. Rep.* **2022**, *12*, 15107. [[CrossRef](#)] [[PubMed](#)]
33. Popov, V.V.; Bagaeva, T.Y.; Otsuji, T.; Ryzhii, V. Oblique terahertz plasmons in graphene nanoribbon arrays. *Phys. Rev. B* **2010**, *81*, 73404. [[CrossRef](#)]
34. Barrios, C.A. Modeling of a Graphene Nanoribbon–based Microfluidic Surface Plasmon Resonance Biosensor. *Plasmonics* **2021**, *17*, 745–752. [[CrossRef](#)]
35. Son, J.G.; Son, M.; Moon, K.-J.; Lee, B.H.; Myoung, J.-M.; Strano, M.S.; Ham, M.-H.; Ross, C.A. Sub-10 nm Graphene Nanoribbon Array Field-Effect Transistors Fabricated by Block Copolymer Lithography. *Adv. Mater.* **2013**, *25*, 4723–4728. [[CrossRef](#)]
36. Gonze, X.; Amadon, B.; Anglade, P.-M.; Beuken, J.-M.; Bottin, F.; Boulanger, P.; Bruneval, F.; Caliste, D.; Caracas, R.; Côté, M.; et al. ABINIT: First-principles approach to material and nanosystem properties. *Comput. Phys. Commun.* **2009**, *180*, 2582–2615. [[CrossRef](#)]
37. Kohn, W. Density-functional theory for excited states in a quasi-local-density approximation. *Phys. Rev. A* **1986**, *34*, 737–741. [[CrossRef](#)]
38. Troullier, N.; Martins, J.L. Efficient Pseudopotentials for Plane-Wave Calculations. *Phys. Rev. B.* **1991**, *43*, 1993. [[CrossRef](#)]
39. Monkhorst, H.J.; Pack, J.D. Special points for Brillouin-zone integrations. *Phys. Rev. B* **1976**, *13*, 5188. [[CrossRef](#)]
40. Geim, A.K.; Novoselov, K.S. The Rise of Graphene. In *Nanoscience and Technology: A Collection of Reviews from Nature Journals*; World Scientific: Singapore, 2010; pp. 11–19.
41. Barone, V.; Hod, O.; Scuseria, G.E. Electronic Structure and Stability of Semiconducting Graphene Nanoribbons. *Nano Lett.* **2006**, *6*, 2748–2754. [[CrossRef](#)]
42. Han, M.Y.; Oezylmaz, B.; Zhang, Y.; Kim, P. Energy Band-Gap Engineering of Graphene Nanoribbons. *Phys. Rev. Lett.* **2007**, *98*, 206805. [[CrossRef](#)]
43. Hwang, C.; Siegel, D.A.; Mo, S.-K.; Regan, W.; Ismach, A.; Zhang, Y.; Zettl, A.; Lanzara, A. Fermi velocity engineering in graphene by substrate modification. *Sci. Rep.* **2012**, *2*, 1–4. [[CrossRef](#)]
44. Zur, A.; McGill, T.C.; Smith, D.L. Fermi-level position at a semiconductor-metal interface. *Phys. Rev. B* **1983**, *28*, 2060–2067. [[CrossRef](#)]
45. Whelan, P.R.; Shen, Q.; Zhou, B.; Serrano, I.G.; Kamalakar, M.V.; Mackenzie, D.M.A.; Ji, J.; Huang, D.; Shi, H.; Luo, D.; et al. Fermi velocity renormalization in graphene probed by terahertz time-domain spectroscopy. *2D Mater.* **2020**, *7*, 035009. [[CrossRef](#)]
46. Pisarra, M.; Sindona, A.; Riccardi, P.; Silkin, V.; Pitarke, J.M. Acoustic plasmons in extrinsic free-standing graphene. *N. J. Phys.* **2014**, *16*, 83003. [[CrossRef](#)]
47. Tene, T.; Guevara, M.; Svozilík, J.; Coello-Fiallos, D.; Briceño, J.; Gomez, C.V. Proving Surface Plasmons in Graphene Nanoribbons Organized as 2D Periodic Arrays and Potential Applications in Biosensors. *Chemosensors* **2022**, *10*, 514. [[CrossRef](#)]

48. Petrakis, L. Spectral line shapes: Gaussian and Lorentzian functions in magnetic resonance. *J. Chem. Educ.* **1967**, *44*, 432. [[CrossRef](#)]
49. Blaber, M.G.; Henry, A.-I.; Bingham, J.M.; Schatz, G.C.; Van Duyne, R.P. LSPR Imaging of Silver Triangular Nanoprisms: Correlating Scattering with Structure Using Electrodynamics for Plasmon Lifetime Analysis. *J. Phys. Chem. C* **2011**, *116*, 393–403. [[CrossRef](#)]
50. Egerton, R.F. Electron energy-loss spectroscopy in the TEM. *Rep. Prog. Phys.* **2008**, *72*, 16502. [[CrossRef](#)]
51. Yang, L.; Park, C.-H.; Son, Y.-W.; Cohen, M.L.; Louie, S.G. Quasiparticle Energies and Band Gaps in Graphene Nanoribbons. *Phys. Rev. Lett.* **2007**, *99*, 186801. [[CrossRef](#)]
52. Ullah, Z.; Witjaksono, G.; Nawi, I.; Tansu, N.; Khattak, M.I.; Junaid, M. A Review on the Development of Tunable Graphene Nanoantennas for Terahertz Optoelectronic and Plasmonic Applications. *Sensors* **2020**, *20*, 1401. [[CrossRef](#)]
53. Kiraly, B.; Mannix, A.J.; Jacobberger, R.M.; Fisher, B.L.; Arnold, M.S.; Hersam, M.C.; Guisinger, N.P. Sub-5 Nm, Globally Aligned Graphene Nanoribbons on Ge (001). *Appl. Phys. Lett.* **2016**, *108*, 213101. [[CrossRef](#)]
54. Ruffieux, P.; Ruffieux, P.; Cai, J.; Cai, J.; Plumb, N.C.; Plumb, N.C.; Patthey, L.; Patthey, L.; Prezzi, D.; Prezzi, D.; et al. Electronic Structure of Atomically Precise Graphene Nanoribbons. *ACS Nano* **2012**, *6*, 6930–6935. [[CrossRef](#)]
55. Elias, D.C.; Gorbachev, R.V.; Mayorov, A.S.; Morozov, S.V.; Zhukov, A.A.; Blake, P.; Ponomarenko, L.A.; Grigorieva, I.V.; Novoselov, K.S.; Guinea, F.; et al. Dirac cones reshaped by interaction effects in suspended graphene. *Nat. Phys.* **2011**, *7*, 701–704. [[CrossRef](#)]
56. Sarker, D.; Nakti, P.P.; Tahmid, I.; Mamun, A.Z.; Zubair, A. Terahertz polarizer based on tunable surface plasmon in graphene nanoribbon. *Opt. Express* **2021**, *29*, 42713. [[CrossRef](#)]
57. Ju, L.; Geng, B.; Horng, J.; Girit, Ç.; Martin, M.; Hao, Z.; Bechtel, H.A.; Liang, X.; Zettl, A.; Shen, Y.R.; et al. Graphene plasmonics for tunable terahertz metamaterials. *Nat. Nanotechnol.* **2011**, *6*, 630–634. [[CrossRef](#)] [[PubMed](#)]
58. Xu, W.; Xie, L.; Zhu, J.; Wang, W.; Ye, Z.; Ma, Y.; Tsai, C.-Y.; Chen, S.; Ying, Y. Terahertz sensing of chlorpyrifos-methyl using metamaterials. *Food Chem.* **2017**, *218*, 330–334. [[CrossRef](#)] [[PubMed](#)]
59. Hua, X.; Qian, G.; Yang, J.; Hu, B.; Fan, J.; Qin, N.; Li, G.; Wang, Y.; Liu, F. Development of an immunochromatographic assay for the rapid detection of chlorpyrifos-methyl in water samples. *Biosens. Bioelectron.* **2010**, *26*, 189–194. [[CrossRef](#)]
60. Xu, W.; Xie, L.; Zhu, J.; Tang, L.; Singh, R.; Wang, C.; Ma, Y.; Chen, H.-T.; Ying, Y. Terahertz biosensing with a graphene-metamaterial heterostructure platform. *Carbon* **2018**, *141*, 247–252. [[CrossRef](#)]
61. Zhou, J.; Zhao, X.; Huang, G.; Yang, X.; Zhang, Y.; Zhan, X.; Tian, H.; Xiong, Y.; Wang, Y.; Fu, W. Molecule-Specific Terahertz Biosensors Based on an Aptamer Hydrogel-Functionalized Metamaterial for Sensitive Assays in Aqueous Environments. *ACS Sensors* **2021**, *6*, 1884–1890. [[CrossRef](#)]
62. Lin, T.N.; Chih, K.H.; Yuan, C.T.; Shen, J.L.; Lin, C.A.J.; Liu, W.R. Laser-ablation production of graphene oxide nanostructures: From ribbons to quantum dots. *Nanoscale* **2015**, *7*, 2708–2715. [[CrossRef](#)] [[PubMed](#)]

Disclaimer/Publisher’s Note: The statements, opinions and data contained in all publications are solely those of the individual author(s) and contributor(s) and not of MDPI and/or the editor(s). MDPI and/or the editor(s) disclaim responsibility for any injury to people or property resulting from any ideas, methods, instructions or products referred to in the content.